Glauconite as a potential paleo-seawater $\delta^{41}K$ proxy archive – Assessing the impacts of sedimentary facies, composition, microstructure and post-depositional alteration

Andre Baldermann[1*], Julius Baumhakel[2], Ralf Ditscherlein[3], Juraj Farkaš[4], Orkun Furat[5,6], Jasmin M. Hiller[4], Matthias Neumann[2], Stefan C. Löhr[4], Urs A. Peuker[3], Volker Schmidt[5] and Xin-Yuan Zheng[7]

[1]Institute of Applied Geosciences, Graz University of Technology & NAWI Graz Geocenter, Austria; baldermann@tugraz.at

[2]Institute of Statistics, Graz University of Technology, Austria; baumhakel@tugraz.at; neumann@tugraz.at

[3]Institute of Mechanical Process Engineering and Mineral Processing, Technische Universität Bergakademie Freiberg, Germany; ralf.ditscherlein@mvtat.tu-freiberg.de; urs.peuker@mvtat.tu-freiberg.de

[4]Metal Isotope Group, Discipline of Earth Sciences, School of Physics, Chemistry and Earth Sciences, Adelaide University, Australia; juraj.farkas@adelaide.edu.au; stefan.loehr@adelaide.edu.au; jasmin.hiller@mymail.unisa.edu.au

[5]Institute of Stochastics, Ulm University, Germany; volker.schmidt@uni-ulm.de

[6]SDU Applied AI and Data Science Unit, University of Southern Denmark, Denmark; ofu@mmmi.sdu.dk

[7]Department of Earth and Environmental Sciences, University of Minnesota–Twin Cities, USA; zhengxy@umn.edu

*Corresponding author: Andre Baldermann

Keywords: Glauconite; Stable K isotopes; Reverse weathering; Marine proxy signatures; Paleo-seawater composition; Diagenesis

Abstract

The stable potassium isotopic composition ($\delta^{41}K$) of seawater can provide important hints on present and past oceanic K cycling, budgets and fluxes, but suitable marine archives recording the pristine seawater $\delta^{41}K$ signature are scarce or prone to post-depositional alteration, such as carbonates and evaporites. Glauconite is a promising alternative archive considering that this authigenic green clay mineral is abundant in the rock record, can now be accurately dated using both bulk fractions and single-grain approaches and forms rapidly during early diagenesis with K^+ sourced primarily from seawater or marine pore fluids. We test the robustness of glauconite as an archive for the $\delta^{41}K$ composition of past seawater against the effects of sedimentary facies, presence of detrital and diagenetic clay mineral inclusions, glauconite maturity, composition and micro-structural properties and degree of weathering of different glauconite fractions. Our assessment integrates X-ray computed tomography coupled with mathematical image analysis, electron microprobe and $\delta^{41}K$ isotope analyses. The studied glauconites were collected from the Langenstein section of Cretaceous age (~121.5 to ~96.1 Ma) in Germany, complemented by coeval GL-O glauconite pellets (~100 to ~95 Ma) from Normandy in France. Although the glauconites (sphericity: 0.74 ± 0.05) exhibit considerably different 1) maturity degrees (slightly evolved to highly evolved; 4.1 to 9.2 wt.% K_2O), 2) total porosities (2 ± 1 to 10 ± 8 vol.%), 3) mean pore volumes (16 ± 11 to 35 ± 51 μm^3), 4) oxidized surface thickness (4 to 10 µm) and 5) clay mineral impurities (up to 12.5 wt.%), the $\delta^{41}K$ composition of all glauconite samples from Langenstein is remarkably uniform at -0.67‰ ± 0.04‰ (n = 10) and also overlaps with the GL-O reference material (-0.68‰ ± 0.03‰, n = 7). This $\delta^{41}K$ signature is isotopically lighter than detrital illite and pore-filling burial illite-smectite (-0.50‰ ± 0.04‰, n = 3), implying preservation of a primary seawater-derived signal. Using the recently constrained K isotope fractionation factor of 0.95‰ (Löhr et al., 2026a) our results suggest that $\delta^{41}K$ of Cretaceous seawater was ~0.2 to 0.3‰ higher than that of modern seawater, implying more intense reverse

weathering under Cretaceous greenhouse conditions. Overall, we conclude that well-preserved glauconite grains are a promising new archive for reconstructing the evolution of seawater $\delta^{41}K$.

1. Introduction

Understanding Earth's systems and ocean chemistry evolution through geological time largely relies on the interpretation of proxy signals (trace elements, isotopes, etc.) recorded in marine sedimentary archives (e.g., Richter et al., 1992; Paytan et al., 1998; Montagna et al., 2008; Wanamaker Jr. et al., 2011; Ellegaard et al., 2020; Steffen et al., 2020; Martin et al., 2022; Lyons et al., 2024). However, many proxies are prone to diagenetic alteration, such as $\delta^{18}O$, $\delta^{13}C$, $\delta^{34}S$ and clumped isotope (Δ_{47}) records in calcareous bio-minerals or marine limestones (e.g., Swart, 2015; Winkelstein and Lohmann, 2016; Fichtner et al., 2017), fluid inclusions in evaporites (e.g., Goldstein, 2001; Mernagh, 2015) and trace element signatures (Sr, Ba, Mn, Fe, etc.) obtained from bulk marine sediment analysis or sequential leachates (e.g., Brand and Veizer, 1980; Banner, 1995; Abanda and Hannigan, 2006; Rafiei et al., 2023). These key uncertainties in proxy records and their preservation challenge the reconstruction of past ocean chemistry and quantification of marine element budgets through time (e.g., Haley et al., 2017; Abbott et al., 2019; Abbott et al., 2022; Löhr et al., 2026b; and references therein).

Variations in the rates of forward silicate weathering (capturing atmospheric CO_2) and reverse weathering (clay mineral authigenesis, which liberates CO_2) serve as important controls on Earth's carbon cycle and thus climate evolution (e.g., Crowley and Berner, 2001; Berner and Berner, 2012; Arvidson et al., 2013; Isson and Planavsky, 2018; Krissansen-Totton and Catling, 2020; Isson and Rauzi, 2024). Silicate weathering and clay mineral neo-formation processes also influence the chemical composition of seawater, such as pH, alkalinity and dissolved alkali and alkaline earth metal concentrations (e.g., Farkaš et al., 2024). The (bio)geochemical cycle of K (concentration: 390 ppm; residence time: ~11 Ma) is closely related to silicate mineral reactions (rather than carbonates) compared to all other major seawater cations, and the precipitation of marine authigenic clay minerals can produce large K isotope fractionation (e.g., Li et al., 2019; Teng et al., 2020; Wang et al., 2020; Zheng et al., 2022a). Thus, the temporal variations of the stable K isotope composition ($^{41}K/^{39}K$ or $\delta^{41}K$) of seawater can most likely provide important information on changes of ocean chemistry, if a suitable marine archive for reconstructing paleo-seawater $\delta^{41}K$ is found (e.g., Santiago Ramos et al., 2018; Li et al., 2019; Zheng et al., 2022a).

However, marine biogenic carbonates (e.g., Li et al., 2021a) and evaporites (e.g., Warren, 2010) have proven to be problematic archives for past seawater $\delta^{41}K$ values. This is mainly due to the incapability of the large K^+ ion to substitute into the carbonate crystal lattice, in addition to generally unconstrained vital effects in K-poor bio-carbonates, as well as restricted stratigraphic abundance of K-rich salts (Löhr et al., 2026a). In this respect, glauconite, $K(Fe^{3+/2+},Al,Mg)_{\Sigma\sim2}[Al_xSi_{4-x}]O_{10}(OH)_2$, can potentially act as a recorder of the past seawater $\delta^{41}K$ composition, because this authigenic mineral phase is K-rich, widespread and easy to recognize in marine sedimentary archives due to its large grain size, green color and favorable magnetic properties that allow a quantitative extraction from the bulk sediment. In addition, glauconite pellets form relatively rapidly (~10^3-10^6 Ma) at the sediment-seawater interface during reverse weathering processes and can be directly dated via $^{40}Ar/^{39}Ar$, K-Ar, Rb/Sr and Ca/K geochronometers (Odin and Matter, 1981; Amorosi, 2012; Banerjee et al., 2016; Rafiei et al., 2023; Baldermann et al., 2022; Scheiblhofer et al., 2022; Rubio and López-Pérez, 2024; Baldermann et al., 2025; Chakraborty et al., 2025; Löhr et al., 2025).

However, before this potentially new and yet untapped seawater $\delta^{41}K$ proxy archive can be applied across geological time (e.g., Banerjee et al., 2016; Rubio and López-Pérez, 2024; Baldermann et al., 2025), its robustness has to be tested against the effects of sedimentary facies, maturity degree, mineralogy, chemical composition, micro-structural characteristics and post-depositional alteration. Here, we use Cretaceous-aged glauconite samples (bulk and sub-fractions) from the well-characterized and precisely dated Langenstein section in Germany and coeval glauconite pellets (the international GL-O reference material) from Normandy in France (e.g., Wilmsen et al., 2005; Baldermann et al., 2017; Baldermann et al., 2022; Scheiblhofer et al., 2022; Löhr et al., 2025) to evaluate the robustness of ancient glauconites as an archive for reconstructing past seawater δ^{41}K composition. Based on our glauconite δ^{41}K isotope datasets we reconstruct the seawater δ^{41}K composition of the late Cretaceous ocean (Early to Middle Cenomanian seawater) and distinguish the marine authigenic green clay δ^{41}K signature from the underlying (‘background’) K isotope signals from terrestrial illite-bearing deposits and/or later diagenetic burial illite-smectite overprints recorded at Langenstein.

2. Materials and methods

2.1 Glauconite sampling, bulk grain separation and single grain collection

Glauconite-bearing sandstone and limestone units (used here to evaluate the glauconite-based marine δ^{41}K proxy) were sampled for this study from the well-characterized Langenstein section (e.g., Wilmsen, 2003; Wilmsen et al., 2005; Baldermann et al., 2017; Baldermann et al., 2022; Scheiblhofer et al., 2022), located in the Subhercynian Cretaceous Basin in Northern Germany (Fig. 1a). In addition, glauconite-free sandstone and conglomerate beds (used here as reference materials for ‘background’ sedimentation to identify detrital and late diagenetic clay mineral δ^{41}K compositions) were sampled from this locality. Thin sections were prepared from all lithotypes (Fig. 1b) using standard procedures.

The Langenstein profile starts with cross-bedded ‘Neocomian’ sandstones of Early Cretaceous age (sample P1; depositional age: ~121.5 Ma). Published K-Ar ages of different grain size fractions acquired from these rocks coupled with illite polytype analysis yielded 247.2 ± 3.4 Ma and 68.0 ± 1.6 Ma for detrital illite and diagenetic illite-smectite, respectively (Baldermann et al., 2017). The ‘Neocomian’ sandstones are unconformably overlain by a ~10-25 cm thin glauconite-free conglomerate of orange-brown (sample P2; ~100.3 Ma, oxidized) to greenish color (sample P3; ~100.3 Ma), corresponding to the ultimus/Aucellina Transgression in the

Early Cenomanian (Ernst et al., 1983). The above ~20 cm thick sandstone layer is rich in glauconite (sample P4_1; ~100.2 Ma; up to 70 wt.%) and was deposited during the Early Cenomanian (lowermost M. mantelli Zone; Scheiblhofer et al., 2022). At the top, this layer or horizon locally weathers into a ~2-5 cm thin, finely crumbled to brittle material, which is rich in glauconite (henceforth called ‘glauconitic grus’; sample P4_2; ~100.2 Ma; 50-70 wt.% glauconite). Up-section, ~3.0 m thick glauconite-bearing limestones (‘Pläner’ Limestones) formed within the lower (sample P5; ~97.5 Ma; 20-30 wt.%) and upper part (sample P6; ~96.8 Ma; 15-20 wt.%) of the M. dixoni Zone of the Early Cenomanian until the A. rhotomagense Zone (sample P7; ~96.1 Ma; < 5 wt.%) of the Middle Cenomanian (Wright and Kennedy, 2017; Scheiblhofer et al., 2022). The pelagic limestones or so-called Poor rhotomagense Limestones, which crop out at the top of the Langenstein section, are glauconite-free and were therefore not considered further in this study.

The glauconite grains were separated as follows: (i) the weakly consolidated glauconite-bearing sandstone (sample P4_1) was disintegrated by mild grinding using mortar and pestle and (ii) the glauconitic limestones (samples P5 to P7) were treated with a 1 M HCl solution to remove the carbonate matrix (Bayon et al., 2023). After washing with MilliQ water and drying at 40 °C, the bulk glauconite fraction was separated from each sample using a neodymium magnet in preparation for chemical and δ^{41}K isotope analysis. After grinding, the < 1 µm size fraction of the glauconite grains from sample P5 was collected using standard sedimentation techniques (sample P5a; ~97.5 Ma) to test the effect of clay mineral impurities, such as illite and illite-smectite, on the δ^{41}K isotopic composition of the glauconite grains (Scheiblhofer et al., 2022). Furthermore, four glauconite sub-fractions (> 100 grains) were separated from sample P6 by hand picking under the optical microscope to verify the effects of glauconite composition, microstructure and surface oxidation/weathering on the preservation of the pristine δ^{41}K isotopic composition: (i) light green pellets (sample P6a), (ii) medium/dark green pellets (sample P6b), (iii) foraminifera test infills (sample P6c) and (iv) oxidized grains (sample P6d).

These (sub-)samples were subjected to chemical/elemental and isotopic δ^{41}K analysis as well as µ-CT measurements. Optical micrographs of all samples are presented in Fig. 1c.

In addition, the international reference glauconite material GL-O was used for comparison, considering its presumably coeval depositional or stratigraphic age with the glauconites from Langenstein (see below and Löhr et al., 2025).

GL-O or GLauconite-Odin reference material was prepared from glauconite-rich calcareous siltstones and sandstones in the basal Cenomanian (stratigraphic age: ~100.2-99.5 Ma) of Normandy in France (Odin 1982). Seven green grain sub-fractions were extracted from bulk GL-O material based on their color and textures (light green; medium and dark green each with and without cracks; very dark green; weathered) and subjected to a detailed petrographic and chemical analysis and in-situ Rb-Sr dating (cf. Figs 1-5 and Table 2 in Löhr et al., 2025). Here, we present the δ^{41}K isotope data from these different GL-O sub-factions as defined above. Note that previous bulk and single grain K-Ar dating yielded GL-O ages of 95.03 ± 1.11 Ma and 101.0 ± 0.3 Ma (Selby, 2009; Hemming et al., 2023), which are thus ~5.5 Ma younger or close to the expected stratigraphic age, respectively. In-situ Rb-Sr dating a yielded a ~10 Ma spread in the different GL-O sub-fractions with a mean age of ~94.8 ± 1.0 Ma (Löhr et al., 2025), thus close to glauconite samples taken from the upper part of the Langenstein section.

2.2 Electron microprobe analyses

The chemical composition of the bulk glauconite fractions (samples P4 to P7) and green grain sub-fractions (samples P6a to P6d) was analyzed by electron microprobe (EMP) analyses using a JEOL JXA-8530F Plus Hyper Probe at the University of Graz (Austria). Samples P4_2 and P5a were not analyzed, because of the small particle size of these powders. Approximately 20 grains were handpicked for each group under an optical microscope and then mounted to produce a diamond polished EpoFix resin mount for EMP analysis. The following analytical conditions were used: 15 keV accelerating voltage, 15 nA beam current and defocused beam,

~3 µm in size. The chemical data were standardized against microcline (Al-Kα, Si-Kα and K-Kα), augite (Mg-Kα and Ca-Kα), ilmenite (Fe-Kα), tugtupite (Na-Kα) and $LaPO_4$ (P-Kα) crystals. Counting times were set to be 10 s on peak and 5 s on background position on each side of the element-specific peak. Only compositions with an analytical error of less than 5 % were considered. The chemical compositions were corrected for the average Fe(II)/Fe(III) ratios of the glauconites reported by Baldermann et al. (2017) based on electron energy-loss spectroscopy (EELS) analyses. Structural formulae (in atoms per formula unit, a.p.f.u.) were calculated based on 22 negative charges (Bailey, 1980), assuming (i) tetrahedral Si + Al equals 4, (ii) Fe, Mg and Al_{rest} are octahedrally bound, (iii) K, Na and Ca occupy the interlayer sites and (iv) P_2O_5 belongs to apatite impurities.

2.3 X-ray computed tomography

X-ray computed tomography (CT) is a non-destructive imaging technique that enables the 3D visualization of internal structures of particles (Maire and Withers, 2014). A polychromatic X-ray spectrum, shaped by the electron acceleration voltage of 80 keV and filtered using a Zeiss standard low energy LE4, was produced. Representative single glauconite pellets from the P6 sub-series were fixed via an adhesive tape for SEM imaging and rotated (360°, 1601 projection images), while projection images were recorded at 15 s exposure time and then reconstructed into a 3D volume. Stacking three samples at the same time allowed all glauconites to be scanned using the same parameters with minimal variation. The attenuation of X-rays within the glauconite pellets depends on their composition and density, as materials with higher atomic number or density absorb more strongly and thus determine the image contrast. It also varies with sample thickness and the properties of the X-ray spectrum, although both parameters are considered constant here due to uniform sample geometry and fixed measurement parameters. The Zeiss Xradia 510 VERSA used in this study is able to reach voxel sizes of ~0.8 µm with detector pixel binning = 2, which is the highest achievable resolution at this instrument (i.e., the smallest voxel size is 800 nm). The 3D volume was reconstructed with the Zeiss proprietary reconstruction software using a standard beam hardening correction of 0.05 and a Gaussian smoothing with parameter sigma = 0.5. To ensure comparability of gray value histograms between samples, a consistent intensity scaling was applied by fixing the upper and lower limits of the histogram. After image reconstruction, the 3D volume was exported as a 16 bit TIFF stack for image post-processing.

2.4 Mathematical image analysis and microstructure characterization

The morphology and microstructure of the glauconite grains were characterized based on the acquired 3D image data. Prior to computing meaningful mathematical descriptors, semantic image segmentation was performed, which classified each voxel either as background, glauconite, rust at the grain surface or pores within the glauconite matrix. After applying a moving average filter to the histogram of greyscale values, the so-called intermodal thresholding was used (Prewitt and Mendelsohn, 1966) to separate the background from the glauconite grains. The resulting segmentation was post-processed in three steps: i) morphological closing with a ball of radius 3 voxel units (VU) (Soille, 1999) was performed on the largest component of the foreground, ii) all voxels that do not belong to the largest component of the background were attached to the foreground and iii) unrealistic surface roughness of the foreground was removed by an erosion with a ball of radius 3 VU, after which all isolated components of the foreground were removed and another dilation with the same structuring element was applied. For computing connected components in binary images, the method bwconncomp implemented in Matlab R2025b was used (MathWorks, 2025).

The pore volume within the glauconite grains was segmented by a Gaussian mixture model (McLachlan and Peel, 2000), where the distribution of greyscale values is modeled by a mixture of two Gaussian distributions each of which represent a class of greyscale values by its mean value and standard deviation. Then, a voxel under consideration was classified by conditioning the mixture distribution on the voxel's greyscale value, followed by determining the class to which it belongs. Finally, morphological closing with a ball of radius 1 VU was applied and all pores that either touch the background or do not protrude into the foreground by more than 2 VU were removed. The oxidized layer at the glauconite surface, which has been determined for one particle per P6 sub-series, was segmented by machine learning. For this purpose, random forests (Breiman 2001) were trained by the software ilastik (Sommer et al. 2011) based on hand-labelled image data. The rust layer determined by the random forest was post-processed by morphological opening and closing of non-rust voxels as well as a subsequent opening of rust voxels. In this step, all morphological operations were performed with a ball of radius 3 VU as structuring element. Rust components smaller than 10^4 voxels were removed and the previously segmented pore volume was separated from the rust layer.

Based on semantic segmentation, global descriptors of the glauconite samples, such as the pore volume, thickness of the rust layer and grain sphericity, were computed. Further, individual pores were segmented to determine the empirical distributions of their size. For this purpose, the segmented pore space was eroded to isolate pore regions that are only connected by a small bottleneck. The remaining connected components are considered as individual pores. Since the pores exhibited different morphologies across the investigated glauconite grains, different radii of 1-2 VU were chosen for the spherical erosion. Volumes and surfaces were computed using the Matlab function regionprops3, which uses the algorithms presented in Legland et al. (2007). Due to spatial porosity gradients towards the boundary of the glauconite grains, the 'inner' porosity, which refers to the part of the particle that has a distance of more than 30 µm to the glauconite particle boundary, was also computed. All data are reported as mean values ± 1SD.

2.5 δ^{41}K isotope analysis via a solution-based CC MC-ICP-MS

Sample preparation was performed in the trace-metal free clean lab facilities in the Department of Earth and Environmental Sciences, University of Minnesota – Twin Cities using high purity chemical reagents, Milli-Q water (18.2 MΩ·cm) and acid-cleaned Savillex Teflon vials. The glauconite grains extracted from Langenstein and GL-O, both bulk and sub-fractions (5-50 mg), were dissolved in mixed concentrated HNO_3 and HF (1:5, v/v) on a Teflon-coated graphite hotplate at 150 °C, followed by concentrated HCl. Fully digested samples were evaporated to dryness and re-dissolved in 0.4 M HCl for purification. Potassium purification was carried out through ion exchange chromatographic separation (Zheng et al., 2022b). The digested samples were passed through a Bio-Rad AG 50W-X8 cation exchange resin (H^+ form, 200-400 mesh) packed in Bio-Rad Poly-Prep columns with a 2 mL resin bed to remove matrix elements. Full recovery of K from the columns ($\geq$ 99%) was achieved using 0.4 M HCl as an eluent and sufficient K purity was ensured by applying the same column separation and purification protocol to each sample twice.

High-precision stable K isotope ratios, $^{41}K/^{39}K$, were measured on a collision-cell (CC) MC-ICP-MS or multi-collector inductively coupled mass spectrometer (Nu Instruments “Sapphire” instrument). Samples (200 to 300 $\mu g \cdot L^{-1}$ K in a 2% HNO_3 matrix) were introduced into the instrument using an Apex Omega HF desolvator and a Teflon nebulizer (uptake rate: ~100 $\mu L \cdot min^{-1}$). Blank 2% HNO_3 solutions were analyzed prior to each $\delta^{41}K$ isotope measurement. The obtained ion intensities for ^{41}K and ^{39}K were subtracted from the subsequent measurement (i.e., on-peak zero correction). All samples were measured by the sample-standard bracketing method using NIST SRM 3141a as the bracketing standard. Potassium concentrations of the samples and bracketing standard were matched within 5% and any analytical bias related to subtle concentration mismatch on $^{41}K/^{39}K$ ratios was corrected using published procedures (Zheng et al., 2022b). Repeated measurements of an in-house high-purity K standard (UMN-K), seawater and the USGS standard BCR-2 were routinely carried out between glauconite sample analyses. The results are expressed by the conventional δ-notation relative to the NIST SRM 3141a standard, according to equation 1:

$$\delta^{41}\mathrm{K} = \left[\frac{(^{41}\mathrm{K}/^{39}\mathrm{K})_{\mathrm{sample}}}{(^{41}\mathrm{K}/^{39}\mathrm{K})_{\mathrm{NIST\ SRM\ 3141a}}} - 1\right] \times 1000 \qquad (1)$$

The obtained results for the standard materials UMN-K (0.43‰ ± 0.04‰), seawater (0.13‰ ± 0.04‰) and BCR-2 (-0.44‰ ± 0.05‰) are consistent with published literature. The estimated long-term precision was better than 0.05‰ (2SD) for δ^{41}K results.

3. Results and interpretation

3.1 Chemical composition of glauconite

The average chemical compositions of the bulk glauconite fractions (samples P4 to P7) and of the separated green grain sub-fractions (P6 sub-series) from the Langenstein section are listed in Table 1. The compositional variability of the glauconite pellets from samples P4 to P7 (reported as the average values) ranges from 51.25–52.68 wt% SiO_2, 6.95–8.42 wt% Al_2O_3, 21.13–23.16 wt% Fe_2O_3, 1.90–2.08 wt% FeO, 4.07–4.30 wt% MgO, 8.73–9.19 wt% K_2O, 0.02–0.03 wt% Na_2O, 0.13–0.51 wt% CaO and 0.10–0.34 wt% P_2O_5, which is indicative of evolved (6–8 wt.% K_2O) to highly evolved (8–10 wt.% K_2O), Fe-rich (>19 wt.% $\sum Fe_2O_3+FeO$) glauconites (Fig. 2a), which host minor apatite inclusions (Amorosi, 2012; Rafiei et al., 2023). No general trend is observed in the chemistry of the glauconites associated with sandstone and limestone lithologies (Table 1), except for a slightly higher Al_2O_3 content of the glauconites in the siliciclastic facies. Thus, the maturity and chemical composition of the glauconite grains vary only slightly from $(K_{0.81-0.87}Ca_{0-0.01})(Fe^{3+}_{1.12-1.24}Fe^{2+}_{0.11-0.12}Al_{0.30-0.36}Mg_{0.43-0.45})_{\sum 2.02-2.03}[Al_{0.33-0.36}Si_{3.64-0.67}O_{10}](OH)_2$ (n = 144) and plot in the documented range of Mesozoic glauconites (Banerjee et al., 2016) and previously published compositions for Langenstein glauconites (Scheiblhofer et al., 2022).

In contrast, the separated green grains from the P6 sub-series are compositionally much more variable (reported as the average values), with 52.71–57.91 wt% SiO_2, 7.16–11.46 wt% Al_2O_3, 17.17–20.58 wt% Fe_2O_3, 2.19–3.63 wt% FeO, 4.02–4.35 wt% MgO, 4.12–7.42 wt% K_2O, 0.17–0.33 wt% Na_2O, 0.25–0.35 wt% CaO and 0.13–0.30 wt% P_2O_5, corresponding to a slightly evolved (4–6 wt.% K_2O) to evolved (6–8 wt.% K_2O) state of glauconite maturity (Fig. 2b). The green grains forming as foraminifera test infillings exhibited the lowest degree of maturity and are thus better described as glauconite-smectite (e.g., Amorosi, 2012; Baldermann et al., 2017). The light green grains are characterized by overall higher Al_2O_3, SiO_2, Na_2O and CaO contents and lower $\sum Fe_2O_3$+FeO and K_2O contents compared to the medium/dark green grains, which is typical for incomplete glauconitization in fecal pellets (e.g., Baldermann et al., 2012; Scheiblhofer et al., 2022). The oxidized grains have moderate K_2O, Al_2O_3, SiO_2 and $\sum Fe_2O_3$+FeO contents (Table 1). The average composition of the green grains from the P6 sub-series varies significantly from $(K_{0.35–0.67}Ca_{0.02–0.03}Na_{0.02-0.04})(Fe^{3+}_{0.85–1.09}Fe^{2+}_{0.12–0.21}Al_{0.31–0.72}Mg_{0.40–0.45})_{\sum 2.06–2.09}[Al_{0.17–0.28}Si_{3.72–0.83}O_{10}](OH)_2$ (n = 47).

The average structural formulae of all glauconite (sub-)samples plot in the dioctahedral domain in the standard charge distribution diagram (Fig. 2c). Except for sample P6c (foraminifera test infillings), which plots as glauconite-smectite, all green grains fall in the compositional field of glauconite (Weaver and Pollard, 1973). The oxidized grains are slightly shifted toward the smectite and glauconite-smectite field (Fig. 2c), which is typical for partly altered glauconite (e.g., Pestitschek et al., 2012). The green grains (reported as the average values) have moderate tetrahedral charges (-0.17 to -0.36 a.p.f.u.), moderate to high octahedral charges (-0.25 to -0.49 a.p.f.u.) and high interlayer charges (0.42 to 0.83 a.p.f.u.), with K^+ as the main interlayer cation (Fig. 2c). They overlap with the composition of the GL-O reference material (cf. Fig. 4 in Löhr et al., 2025). The plot of the chemical data in the $nSi^{4+}/4$ vs ^{VI}Fe diagram reveals an evolution from Fe^{3+}-smectite and glauconite-smectite to glauconite end-member composition (Fig. 2d).

3.2 Glauconite grain morphology and microstructure

Mean values (±1SD) of morphological and microstructural descriptors of the glauconite grains from the P6 sub-series are reported in Table 2. Statistical analysis of CT-derived 3D image data shows that the glauconite grains have a rounded particle shape (sphericity: 0.74 ± 0.01; Fig. 3a) and an oxidative layer at the grain surface, 1.3 to 4.5 µm thick, with the greatest thickness observed on sample P6d (Fig. 3b). Highest total and inner porosities were recognized in the light green pellets (P6a: 10-11 vol.%) and in the foraminifer test infills (P6c, Hedbergella: 8-9 vol.%), whereas the medium to dark green pellets and the inner part of the oxidized pellets yielded the lowest total and inner porosities (P6b and P6d$_i$, which are still larger than 2 vol.%). The bulk oxidized pellets had an intermediate porosity (P6d: 4 vol.%) due to the dense inner pore structure and the presence of a highly porous transitional zone toward the oxidized rim (marked as 'core' and 'rim' in Fig. 3b). Accordingly, largest mean and inner pore volumes were observed in samples P6a (24-27 µm^3), P6c (35-52 µm^3, which also yielded the highest variability) and P6d$_i$ (28 µm^3) and the smallest ones in samples P6b (9-16 µm^3) and P6d (8 µm^3). This suggests a densification of the pore structure as 'boxwork-like networks' of Fe-smectite (~10-20 vol.%) evolve to 'rosette-like structures' of glauconite (~5-10 vol.%), consistent with Baldermann et al. (2013), whereas reverse glauconitization creates more open pore networks at the oxidized surface.

3.3 Potassium isotope (δ^{41}K) variations

The measured δ^{41}K values of the samples from the Langenstein section are listed in Table 3, together with the δ^{41}K values of the GL-O sub-fractions. The glauconite-free sedimentary strata from Langenstein (Neocomian sandstones and basal conglomerate) containing illite and illite-smectite have a δ^{41}K composition between -0.46 ± 0.05‰ and -0.51 ± 0.04‰ (Fig. 4a), consistent with a Bulk Silicate Earth (BSE: -0.43 ± 0.17‰) or Upper Continental Crust (UCC: -0.44 ± 0.05‰) signature (e.g., Huang et al., 2020; Wang et al., 2021). Up-section, the δ^{41}K values of the glauconite grains extracted from the glauconite-bearing interval (samples P4 to P7) are~0.18‰ lower, averaging -0.66 ± 0.04‰. No isotope variation is observed between glauconites hosted in sandstone vs limestone lithologies (Fig. 4a). Given that marine glauconite typically forms relatively rapidly (>400 kyr) and in close proximity to the sediment-seawater interface in shelfal sequences, a seawater-derived K^+ source for glauconite including the studied glauconite-bearing lithologies is thus very likely (e.g., Wilmsen and Bansal, 2021; Tribovillard et al., 2023; Löhr et al., 2026a). Interestingly, sub-sample P5a (glauconite with a particle size smaller than 1 µm), which contains the highest amount of clay mineral impurities based on previously reported quantitative XRD analysis (Scheiblhofer et al., 2022), yielded identical δ^{41}K values (-0.67 ± 0.03‰; Fig. 4a). The partially altered samples P4_2 (glauconite grus) and P6d (oxidized glauconite pellets) have slightly lower δ^{41}K values of -0.71 ± 0.05‰ (Fig. 4a,b), which, however, still overlap with the bulk glauconite grains (-0.66 ± 0.04‰) within analytical uncertainty. Similarly, all green grains from the P6 sub-series fall in the same range as the bulk glauconite fractions, averaging -0.66 ± 0.03‰ (Fig. 4b). The approximately time-equivalent GL-O sub-fractions have a δ^{41}K composition between -0.80 ± 0.02‰ and -0.63 ± 0.03‰, with a mean of -0.68 ± 0.03‰, which thus also overlaps with the δ^{41}K values measured in the Langenstein glauconites (Fig. 4a). No systematic δ^{41}K isotope trends are observed within individual GL-O grains.

4. Discussion

4.1 Lithotypes containing K-bearing clays at Langenstein

Four lithotypes containing detrital, early diagenetic (i.e., authigenic in the sense of reverse weathering) and burial diagenetic K-bearing minerals were identified across the Langenstein profile in Northern Germany (Fig. 1a,b).

Lithotype 1 is represented by cross-bedded Neocomian sandstones of yellowish-grayish-brown color, which comprise quartz, illite, chlorite, kaolinite, orthoclase and albite as well as minor calcite spar, Fe-(hydr)oxide cement and illite-smectite (cf. sample P1 in Fig. 1b). Due to the absence of marine faunal elements, these rocks were interpreted as fluviatile deposits (Wilmsen, 2007). Previous studies found that illite (5-8 wt.%) is R3-ordered with a $2M_1$ polytype structure and that diagenetic illite(60)-smectite(40) (1-2 wt.%) has a $1M_d$ polytype structure (R1-ordered) (Baldermann et al., 2017). This indicates that $2M_1$ illite is detrital in origin and simply reflects background sedimentation (Grathoff and Moore, 1996), as confirmed by its 'old' age (247.2 ± 3.4 Ma), relative to the depositional age of the Neocomian sandstones (~121.5 Ma). In contrast, $1M_d$ illite-smectite occurs as a pore fill or replaces feldspar grains, which is typical of a burial diagenetic origin (Huang et al., 1986; Grathoff and Moore, 1996), consistent with its 'younger' age (68.0 ± 1.6 Ma), compared to the Neocomian sandstones.

Lithotype 2 is characterized by an orange-brown to greenish conglomerate (cf. samples P2 and P3 in Fig. 1b), which contains quartz, sandstone pebbles, dolomitic limestone, Fe(hydr)oxide crusts and illite as well as illite-smectite, phosphorite granules and Fe-(hydr)oxide cement. This bed has been interpreted as a basal marine transgression conglomerate, which formed during the ultimus/Aucellina Transgression in the Early Cenomanian (Ernst et al., 1983). Given that illite (6-7 wt.%) and illite-smectite (3 wt.%) share similar textural features compared to the clay mineral assemblage in lithotype 1 (Baldermann et al., 2017), an identical source/origin of the two clay types can be inferred, i.e., detrital vs burial diagenetic.

Lithotype 3 is a sandstone bed containing up to 70 wt.% glauconite (cf. sample P4 in Fig. 1b), in addition to silicate detritus (quartz, siliceous lithoclasts, illite and feldspar, ~20 wt.% in total) and minor calcite spar, micrite and Fe-(oxy)hydroxide cement. The presence of shell debris, the high detritus content and the presence of bio-apatite grains suggest deposition in a proximal shelf setting at the onset of the Early Cenomanian transgression (Wilmsen, 2007). The green grains are intact, not corroded or oxidized and contain slightly elevated Al_2O_3 contents (Fig. 2c,d), which is all typical for authigenic glauconites that formed via replacement of silicate detritus-rich fecal pellets during early diagenesis, without significant subsequent reworking (e.g., Banerjee et al., 2016; Chakraborty et al., 2025). Further, published XRD data reveal that the glauconites have ~95% glauconite layers and ~5% smectite layers (R3-ordered) with a dominant 1M polytype structure (Baldermann et al., 2017), which is indicative of *in-situ* glauconitization close to the sediment-seawater interface.

Lithotype 4 expresses as micritic limestones with decreasing glauconite (26 to ~12 wt.%) and silicate detritus (16 to 13 wt.%) content up-section (cf. samples P5-7 in Fig. 1b), with the latter comprising quartz, feldspar, apatite, kaolinite, illite and illite-smectite (Baldermann et al., 2017; Scheiblhofer et al., 2022). These glauconite-bearing limestones formed in a mid-to-outer shelf setting, as inferred from index ammonites as well as documented and calcisphere assemblages (Wilmsen, 2007). The green pellets are (sub)rounded, while green clays infilling foraminifera tests preserve the original shape of the bio-substrates in which they have formed. All glauconite grains are neither broken nor oxidized and contain slightly elevated $\sum Fe_2O_3+FeO$ over Al_2O_3 contents (Fig. 2a,c,d), implying a formation und suboxic conditions, which is typical for marine glauconites forming in silicate detritus-poor distal shelf settings (e.g., Odin and Matter, 1981; Rubio and López-Pérez, 2024). These glauconites have more than 95% glauconite layers (R3-ordered) and a dominant 1M polytype structure, which is typical for an *in-situ* glauconitization process (Baldermann et al., 2017).

Taken together, the Langenstein profile comprises sandstone and conglomerate beds at the base, which contain different proportions of detrital illite, burial diagenetic illite-smectite and K-feldspar. Up-section, the amount of these K-bearing minerals decreases gradually in the bulk sediments in favor of authigenic glauconites hosted in proximal sandstone and distal limestone facies. However, the glauconite-bearing strata still contain minor amounts of the other K-rich phases that are inherited from the proximal siliciclastic facies (< 2 wt.% each). Below, we discuss the effects of the presence of detrital and diagenetic clay mineral impurities in glauconite, the degree of glauconite maturity, the microstructure of glauconite and the weathering intensity of glauconite on its $\delta^{41}K$ signature in order to test whether glauconite can serve as a reliable recorder of paleo-seawater K isotope composition.

4.2 Clay mineral impurities in Langenstein glauconites

Well crystallized $2M_1$ illite and poorly crystallized $1M_d$ illite-smectite account for 1-2 wt.% and 3-11 wt.% in the separated bulk glauconite fractions, with the highest clay mineral impurity content found in samples P5 and P5a (12.5 wt.%) and the lowest one in sample P4 (5 wt.%; Scheiblhofer et al., 2022). Although the K_2O contents of these detrital and diagenetic clays were determined to be as high as 8.3 ± 0.4 wt.% and 4.5 ± 0.5 wt.%, respectively (Baldermann et al., 2017), no effect on the $\delta^{41}K$ composition of the bulk glauconite grains from samples P4 to P7 was evident within analytical precision of the $\delta^{41}K$ isotope measurements (cf. Fig. 5, Fig. 4a and Table 3). This is probably because K-bearing phases other than glauconite are relatively scarce in the bulk green grains and the K_2O content of glauconite is very high (8.7-9.2 wt.%; Table 1), so that a shift toward isotopically heavier $\delta^{41}K$ signatures of the green grains caused by the presence of small/moderate amounts of K-bearing impurities is negligible (Fig. 5).

If we consider the average Langenstein glauconite $\delta^{41}K$ signature of -0.66 ± 0.04‰ (samples P4 to P7) and account for the $\delta^{41}K$ composition of the detrital silicate input of sample P1 of -0.46 ± 0.05‰ (Table 3), which has the highest illite (6 wt.%) and K-feldspar (2 wt.%) contents and the lowest illite-smectite (2 wt.%) content, the 'pure' glauconite grains would have a $\delta^{41}K$ composition of -0.68 ± 0.05‰. This is almost identical to the measured $\delta^{41}K$ values of the bulk Langenstein grains and/or coeval GL-O glauconite pellets (Table 3). Similarly, excluding the contribution of the K-bearing phases from sample P5 ($\text{glauconite}_{\text{AVG\_P5}}$ $\delta^{41}K$ = -0.68 ± 0.04‰), which contains a high illite-smectite (11 wt.%) content and low illite (1.5 wt.%) and K-feldspar (1 wt.%) contents ($\text{silicate}_{\text{AVG\_P1-3}}$ $\delta^{41}K$ = -0.50 ± 0.04‰), would result in a 'pure' glauconite $\delta^{41}K$ composition of -0.71 ± 0.07‰, thus still overlapping with the measured $\delta^{41}K$ values of the bulk grains within analytical precision (Table 3). The same holds true for sub-sample P5a (< 1 µm), suggesting that the particle size does not impact the bulk glauconite $\delta^{41}K$ isotope composition (Table 3).

We note that we could not measure the δ^{41}K composition of pure illite and pure illite-smectite in our samples, because the two phases are likely intergrown. However, plotting the fractions of illite and K-feldspar (10 and 7.5 wt.%) against the δ^{41}K composition of samples P1 (-0.46‰) vs P2 and P3 (-0.51‰) results in an illite-smectite δ^{41}K signature of -0.64%, which is close to the bulk glauconite δ^{41}K composition (Table 3). This could indicate that both glauconite and illite-smectite phases precipitated from a compositionally similar paleo-seawater or marine pore fluid source, which inherited the K isotope composition of Cretaceous seawater, being (slightly) modified by detrital silicate (e.g., feldspar) dissolution reactions that took place in the ancient sediment pile (Li et al., 2022). This view is supported by the well-documented uptake of light ^{39}K isotopes during clay mineral formation and sediment diagenesis (Li et al., 2019), findings of diagenetic illite-smectite replacing K-feldspar grains (Fig. 1b) and kinetic modeling of the thermal history at Langenstein, which yielded a shallow burial depth of 1000-1500 m and a low burial temperature of 50-65 °C to form the diagenetic illite-smectite (Baldermann et al., 2017). We therefore conclude that small proportions of detrital 'K-rich' phase impurities and moderate amounts of 'K-poor' mixed layered clay mineral impurities in glauconite grains do not disturb significantly the seawater-derived pristine glauconite δ^{41}K signature (Fig. 5), consistent with observations reported for modern glauconites and glauconite-smectite (Löhr et al., 2026a).

4.3 Maturity degree of Langenstein glauconites

Our EMP data reveal that the glauconite pellets (samples P4 to P7) are compositionally evolved to highly evolved (cf. Fig. 2a and Table 1), judged from their K_2O contents (Amorosi, 2012), and plot well within the compositional range of other Mesozoic glauconites (Banerjee et al., 2016). In contrast, the separated green grains from the P6 sub-series are slightly evolved to evolved (cf. Fig. 2b and Table 1), corresponding to a glauconite-smectite composition rather than the glauconite member (Fig. 2c,d). Nevertheless, the δ^{41}K compositions of all glauconitic samples from Langenstein fall within a very close range (Fig. 4a,b), averaging -0.67 ± 0.04‰.

No correlation is observed between the K_2O contents of the glauconite grains from Langenstein and also GL-O pellets and their $\delta^{41}K$ signatures (Fig. 6). This suggests that glauconite layers can record of the pristine seawater $\delta^{41}K$ signature if the K_2O content in glauconite-smectite exceeds a certain threshold value, which is 4 wt.% or even lower according to our datasets (cf. Table 1 and 3). However, extremely low K_2O contents in mixed-layered glauconite-smectite would result in higher proportions of smectite layers and such K-bearing smectite layers are still prone to ion exchange reactions (e.g., Mosser-Ruck et al., 2001), with implications for possible resetting and/or overprint of K isotopes (Li et al., 2021b). In line with previous studies, hydrothermal experiments conducted at 250°C for 10 h have shown that Ar degassing and resetting of the Rb-Sr system are significantly reduced once K_2O contents of glauconitized fecal pellets exceed ~4.3 wt.% (Bonhomme and Odin, 1979; Clauer, 1981).

Using the published relation between the interlayer K^+ content (in a.p.f.u.) and the proportion of glauconite layers in interstratified glauconite-smectite, as it progressively evolves toward the glauconite member (Baldermann et al., 2013), indicates that the majority of the green grains from Langenstein (and also GL-O) already contain ~90% to 100% glauconite layers, thus corresponding to a very high degree of maturity (Fig. 2a,b). Exceptions are the sub-samples P6c (67%) and P6d (88%), which reflect incomplete glauconitization of foraminifers and partial oxidative alteration of some glauconite pellets (Fig. 2b), respectively, though their degree of glauconitization is still moderate to high. This could imply that once a certain degree of glauconitization is reached, K^+ ions are 'locked' within the nonexchangeable interlayer sites. As a result, the glauconite $\delta^{41}K$ signature may become resistant to subsequent ion exchange or isotopic resetting during interaction with burial fluids or other post-depositional alterations.

4.4 Microstructure of Langenstein glauconites

Our statistical analysis of 3D image data produced meaningful morphological and structural descriptors, such as total porosity, sphericity, pore volume and thickness of oxidative crusts, for chemically pre-screened (Fig. 2b) and carefully selected individual glauconite grains (cf. Fig. 1c and 3, Table 2). Changes of any of these parameters during glauconite maturation or post-depositional alteration have the potential to alter the pristine K isotope composition of marine authigenic glauconite, for example, via incomplete glauconitization. The latter could lead to delayed isotopic closure (Löhr et al., 2025), (de)sorption or ion exchange reactions occurring at the glauconite surface (Li et al., 2021b), progressive alteration of glauconite into secondary (clay) minerals (Pestitschek et al., 2012) or resetting of K isotopes during interaction with burial fluids (Loyola et al., 2025). In this respect, changes in porosity and pore volume as well as the presence of alteration layers during post-depositional evolution of glauconites need to be better constrained to evaluate their potential effects on the K isotope composition of glauconite.

Our statistical analysis of 3D image data obtained from individual glauconite grains from the P6 sub-series yielded total porosities between 2 ± 1 and 10 ± 8 vol.%, inner porosities between 1 ± 0.3 and 11 ± 10 vol.%, mean pore volumes between 16 ± 11 and 35 ± 5 µm³ and oxidized crust thicknesses ranging from 4 to more than 10 µm (Table 2). Despite this large variability in morphological and microstructural properties, the K isotope composition of these individual glauconite grains remained almost constant within analytical uncertainty, ranging from -0.66‰ to -0.71‰, with an average of 0.68‰ ± 0.03‰ (Fig. 7a-c). This signature is indistinguishable from that of the bulk glauconite fraction (-0.66‰ ± 0.02‰) (Fig. 4), supporting the view that interstratified glauconite-smectite with K_2O contents of ~4 wt.% (or even lower) can preserve the pristine seawater $\delta^{41}K$ signature. Follow up studies are required to evaluate if the pristine glauconite $\delta^{41}K$ signature is preserved when they get exposed to compositionally different and hotter burial fluids. However, based on our results we conjecture that microstructural variation in individual glauconite grains that have been exposed to a moderate degree of burial diagenesis (~1000-1500 m depth and 50-65 °C) do not have a significant impact on the pristine K isotope composition of glauconite.

4.5 Chemical weathering of Langenstein glauconites

Oxidative weathering of glauconite-bearing deposits is often expressed by modifications in color, mineralogy and chemistry of the initially dark green grains. For example, glauconites that were subjected to intense chemical weathering in an arid climate in Egypt for up to 42 years developed a brownish-green color and showed decreased concentrations of Fe_2O_3 and K_2O but increased Al_2O_3 and SO_4 concentrations as well as mineralogical change toward mixed-layered illite-smectite with up to 50% expandable smectite layers and pure smectite (Pestitschek et al., 2012). Similar alteration trends are observed at Langenstein: sample P4_2 transformed into a loose glauconitic grus of greyish-greenish-brown color. It was not possible to determine the chemical composition of this glauconitic weathering product by EMP analysis, because of the small particle size. However, the broadening of the *00l*-reflections, the decreasing intensity of the polytype diagnostic peaks at 3.65 Å and 3.09 Å and the presence of a 15 Å peak all point to oxidative alteration of the glauconite grains (Fig. 8) and their progressive weathering into Fe-rich illite-smectite and Al-rich smectite (Kisiel et al., 2018). Similar XRD patterns were obtained for the partially altered glauconite pellets from sample P6d (Fig. 8), which exhibited Fe-(hydr)oxide crusts (Fig. 1c, 3b) and reduced concentrations of $\sum Fe_2O_3$+FeO (-10.0%), MgO (-3.0%) and K_2O (-27.2%) but higher Al_2O_3 (+15.5%) and SiO_2 (+4.5%) contents (Table 1), compared to sample P6. These chemical changes shift its composition toward the smectite and glauconite-smectite fields (Fig. 2c). Nevertheless, the $\delta^{41}K$ signature of the altered samples was indistinguishable from all unaltered glauconite samples within analytical uncertainty (Table 3). This observation suggests that a mild degree of oxidation does not affect the $\delta^{41}K$ signature of glauconite. Still, partial dissolution of the octahedral layer and intense leaching of interlayer cations is thought to liberate Al^{3+}, Mg^{2+}, $Fe^{3+/2+}$ and K^+ ions from the glauconite crystal lattice, which may modify the $\delta^{41}K$ signature of glauconite during 'reverse glauconitization' in the long term (e.g., Courbe et al., 1981; Hassan and Baioumy, 2006; Sánchez-Navas et al., 2008).

4.6 Implications for glauconite as an archive for paleo-seawater $\delta^{41}K$

Chemical weathering of silicate rocks delivers K^+ to the oceans, regulating global K fluxes and isotopic budgets in various K reservoirs on Earth's surface (e.g., Li et al., 2021b). Thus, the total oceanic K budget and its isotope composition ($\delta^{41}K$) is primarily controlled by the K fluxes from continental runoff and groundwater discharge, hydrothermal inputs generated at mid-oceanic ridge sites and K sequestration by low-temperature hydrothermal alteration of seafloor and formation of marine authigenic (clay) minerals (e.g., Santiago Ramos et al., 2018; Li et al., 2019). It is well established that the Bulk Silicate Earth has an isotopically lighter K isotopic composition (BSE: -0.43 ± 0.17‰; UCC: -0.44 ± 0.05‰; Huang et al., 2020; Wang et al., 2021) than modern seawater ($\delta^{41}K_{seawater}$ = ~+0.134‰; Hille et al., 2019). Major K sources in the modern ocean, including rivers and mid-ocean ridge hydrothermal inputs, have global average $\delta^{41}K$ values of ~-0.3‰ (Li et al., 2029; Wang et al., 2021; Zheng et al., 2022; Santiago Ramos et al., 2022), which are only slightly higher than that of the BSE, and thus cannot account for the heavy K isotope signature of seawater. Although low-temperature hydrothermal alteration preferentially sequestrates light K isotopes from seawater into altered material, the associated K isotope fractionation is not sufficient to explain the full $\delta^{41}K$ difference of ~0.6‰ between seawater and BSE (Hu et al., 2020; Liu et al., 2021). Increasingly, K fixation during marine clay mineral authigenesis has been postulated as an essential process in controlling the global oceanic K isotope mass balance (e.g., Li et al., 2021b; Zheng et al., 2022).

Glauconite is a particularly important candidate mineral in this respect due to its high abundance in marine sediments and its high K contents (Baldermann et al., 2025). Direct measurements of authigenic glauconite grains from core-top marine sediments have confirmed that glauconite formation strongly incorporates light K isotopes from seawater, yielding $\delta^{41}K$ values that are ~0.95‰ lower than modern seawater (Löhr et al., 2026a). The $\delta^{41}K$ dataset obtained from the Cretaceous glauconites from two paleo-locations (Germany and France) indicates that ancient and well-preserved glauconite grains can indeed record and preserve the pristine paleo-seawater

δ^{41}K signal and is not significantly impacted by potential modifying influences, such as varying facies, K-bearing mineral impurities, diverse maturity and microstructural properties and the degree of oxidative weathering. However, any robust reconstruction of paleo-seawater δ^{41}K composition based on the K isotope analysis of ancient glauconite grains relies on the seawater-glauconite ($\Delta^{41}K_{seawater\text{-}glauconite}$) fractionation factor (Löhr et al, 2026a) and its validation by future studies.

Encouragingly, the recent progress made in the separation and quantification of Fe(III)-smectite and glauconite in modern marine sediments from two contrasting sites (equatorial Atlantic vs NE Pacific) have yielded nearly identical glauconitic/green clay δ^{41}K values of -0.8‰ ± 0.1‰, which can be thus translated to a globally representative $\Delta^{41}K_{seawater\text{-}glauconite}$ of ~0.95‰ (Löhr et al., 2026a). Applying this $\Delta^{41}K_{seawater\text{-}glauconite}$ fractionation factor to the Langenstein glauconites and GL-O grains gives an isotopically heavier (ca. 0.24‰ to 0.31‰) δ^{41}K composition of the Cenomanian seawater compared to present-day seawater. The Cretaceous greenhouse world was characterized by enhanced continental weathering and faster seafloor spreading relative to today (e.g., Jones and Jenkyns, 2001; Seton et al., 2009; Jenkyns, 2010; Müller et al., 2022) but higher weathering and hydrothermal input fluxes should lower the global seawater δ^{41}K value and drive it toward the BSE value. Therefore, the isotopically heavier or higher δ^{41}K value of mid-Cenomanian seawater, as inferred from the Langenstein glauconites and coeval GL-O pellets, likely imply enhanced marine clay authigenesis or marine reverse weathering under prolonged Cretaceous greenhouse conditions (Baldermann et al., 2022). This process thus has had potentially important implications for the marine C cycle, ocean chemistry and the oceanic alkalinity budget and thus Earth's climate stability during this time (e.g., Isson and Planavsky, 2018. Farkaš et al., 2024 and references therein).

5. Conclusions

Bulk grains and various sub-fractions of glauconite were separated from marine shelfal deposits of Cretaceous age in Germany (Langenstein section) and France (GL-O from Normandy) based on color, morphology/texture, state of oxidation/weathering and type of replacement in order to evaluate the robustness of glauconite as a seawater δ^{41}K archive. The effects of sedimentary facies, detrital and diagenetic clay inclusions, glauconite maturity, composition, microstructure and post-depositional alteration on the glauconite δ^{41}K signatures were assessed. We used X-ray computed tomography with statistical image analysis, electron microprobe measurements and δ^{41}K isotope analyses for the characterization of the separated glauconites, which yielded a large variation in K_2O content (4.1–9.2 wt.%), total porosity (2–10 vol.%), pore volume (16–35 µm^3), oxidized grain thickness (4–10 µm) and clay mineral impurities (up to 12.5 wt.%) within both bulk and individual glauconite grains. Despite these large differences all glauconite samples from Langenstein and GL-O displayed uniform δ^{41}K values of −0.67‰ ± 0.04‰ and −0.68‰ ± 0.03‰, respectively, indicating preservation of a primary seawater- or marine pore water-derived K isotope signal. Applying a K isotope fractionation factor of 0.95‰ between modern seawater and recent glauconite-smectite, our results suggest that the Cretaceous $K_{seawater}$ isotope composition was ~0.2–0.3‰ higher than today. This finding suggests that authigenic green clay formation or reverse silicate weathering was enhanced under Cretaceous greenhouse conditions, with potential implications for ocean chemistry, the marine C cycle and thus Earth's climate at this time. We conclude that well-preserved glauconite is a promising new archive for reconstructing past seawater δ^{41}K.

Data availability

All data are available within the article.

CRediT authorship contribution statement

Andre Baldermann: Conceptualization, Funding acquisition, Formal analysis, Investigation, Methodology, Visualization, Writing – original draft, Writing – review & editing. **Julius Baumhakel:** Methodology, Visualization, Writing – review & editing. **Ralf Ditscherlein:** Methodology, Visualization, Writing – review & editing. **Juraj Farkaš:** Writing – review & editing. **Orkun Furat:** Methodology, Visualization, Writing – review & editing. **Jasmin M. Hiller:** Writing – review & editing. **Matthias Neumann:** Methodology, Visualization, Writing – review & editing. **Stefan C. Löhr:** Writing – review & editing. **Urs A. Peuker:** Writing – review & editing. **Volker Schmidt:** Methodology, Writing – review & editing. **Xin-Yuan Zheng:** Formal analysis, Methodology, Visualization, Writing – review & editing.

Declaration of competing interest

The authors declare that they have no known competing financial interests or personal relationships that could have appeared to influence the work reported in this paper.

Acknowledgements

This work was financially supported by the NAWI Graz, the ARC Discovery Project (DP210100462; grant to JF, AB and SCL) titled 'Glauconite: Archive Recording the Timing and Triggers of Cambrian Radiation', the Horizon Europe EXCITE^2 project (E2-C1_111; grant to AB) and a NSF CAREER award (#2238685; grant to XZ). This article is based upon work from COST Action mSPACE, CA24122, supported by COST (European Cooperation in Science and Technology). Open access funding was from the Graz University of Technology.

References

Abanda, P.A., Hannigan, R.E., 2006. Effect of diagenesis on trace element partitioning in shales. Chem. Geol. 230, 42–59.

Abbott, A.N., Löhr, S.C., Payne, A., Kumar, H., Du, J., 2022. Widespread lithogenic control of marine authigenic neodymium isotope records? Implications for paleoceanographic reconstructions. Geochim. Cosmochim. Acta. 319, 318–336.

Abbott, A.N., Löhr, S.C., Trethewy, M., 2019. Are clay minerals the primary control on the oceanic rare earth element budget? Front. Mar. Sci. 6, 1–19.

Amorosi, A., 2012. The occurrence of glaucony in the stratigraphic record: distribution patterns and sequence stratigraphic significance. International Association of Sedimentologists Special Publications, 45, 37–54.

Arvidson, R.S., Mackenzie, F.T., Guidry, M.W., 2013. Geologic history of seawater: A MAGic approach to carbon chemistry and ocean ventilation. Chem. Geol. 362, 287–304.

Baldermann, A., Banerjee, S., Czuppon, G., Dietzel, M., Farkaš, J., Löhr, S., Moser, U., Scheiblhofer, E., Wright, N.M., Zack, T., 2022. Impact of green clay authigenesis on element sequestration in marine settings. Nat. Commun. 13, 1527.

Baldermann, A., Banerjee, S., Löhr, S.C., Rudmin, M., Warr, L.N., Chakraborty, A., 2025. Exploring reverse silicate weathering across geological time: a review. Clay Miner. 60, 1–27.

Baldermann, A., Dietzel, M., Mavromatis, V., Mittermayr, F., Warr, L.N., Wemmer, K., 2017. The role of Fe on the formation and diagenesis of interstratified glauconite-smectite and illite-smectite: A case study of Upper Cretaceous shallow-water carbonates. Chem. Geol. 453, 21–34.

Baldermann, A., Grathoff, G.H., Nickel, C., 2012. Micromilieu-controlled glauconitization in fecal pellets at Oker (Central Germany). Clay Miner. 47, 513–538.

Baldermann, A., Stamm, F.M., Farkaš, J., Löhr, S., Ratz, B., Letofsky-Papst, I., Dietzel, M., 2024. Precipitation of short-range order hydroxy aluminosilicate (HAS) and hydrous ferric silicate (HFS) at ambient temperature: Insights into mineral formation pathways, crystal chemistry and solubility-stability relationships. Chem. Geol. 646, 121911.

Baldermann, A., Warr, L.N., Grathoff, G.H., Dietzel, M., 2013. The rate and mechanism of deep-sea glauconite formation at the Ivory Coast – Ghana marginal ridge, Clays Clay Miner. 61, 258–276.

Banerjee, S., Bansal, U., Thorat, A.V., 2016. A review on palaeogeographic implications and temporal variation in glaucony composition. J. Palaeogeogr. 5, 43–71.

Banner, J.L., 1995. Application of the trace element and isotope geochemistry of strontium to studies of carbonate diagenesis. Sedimentology 42, 805–824.

Bayon, G., Giresse, P., Chen, H., Rouget, M.-L., Gueguen, B., Moizinho, G.R., Barrat, J.-A., Beaufort, D., 2023. The Behavior of Rare Earth Elements during Green Clay Authigenesis on the Congo Continental Shelf. Minerals 13, 1081.

Berner, E.K., Berner, R.A., 2012. Global Environment: Water, Air, and Geochemical Cycles. Princeton University Press, Princeton, 1–443.

Bonhomme, M.G., Odin, G.S., 1979. Isotopic consequences of preheating in potassium-argon dating of various glauconies. 6th European Colloquium Geochronology, Lillehammer, Norway, 1–9.

Brand, U., Veizer, J., 1980. Chemical diagenesis of a multicomponent carbonate system; 1, Trace elements. J. Sediment. Res. 50, 1219–1236.

Breiman, L., 2001. Random forests. Mach. Learn. 45, 5–32.

Chakraborty, A., Srivastava, A., Singh, B., Punekar, J., Dasgupta, S., Chakrabarty, S., Banerjee, S., 2025. Oxygen-depleted and ferruginous seawater composition imprinted in Early Cretaceous Fe-rich Al-glauconites in marginal marine deposits. Sci. Rep. 15, 37208.

Clauer, N., 1981. Rb-Sr and K-Ar dating of Precambrian clays and glauconites. Precam. Res. 15, 331–352.

Courbe, C., Velde. B., Meunier. A., 1981. Weathering of glauconites: reversal of the glauconitization process in a soil profile in western France. Clay Miner.16, 231–243.

Crowley, T.J., Berner, R.A., 2001. CO_2 and Climate Change. Science 292, 870–872.

Ellegaard, M., Clokie, M.R.J., Czypionka, T., Frisch, D., Godhe, A., Kremp, A., Letarov, A., McGenity, T.J., Ribeiro, S., Anderson, N.J., 2020. Dead or alive: sediment DNA archives as tools for tracking aquatic evolution and adaptation. Commun. Biol. 3, 169.

Farkaš, J., Wallmann, K., Mosley, L., Staudigel, P., Zheng, X.-Y., Leyden, E., Shao, Y., Fryda, J., Holmden, C., Eisenhauer, A., 2024. Alkalinity and elemental cycles in present and past ocean: Insight from geochemical modeling and alkali and alkaline earth metal isotopes. Treatise on Geochemistry (Third Edition), pp. 33-87.

Fichtner, V., Strauss, H., Immenhauser, A., Buhl, D., Neuser, R.D., Niedermayr, A., 2017. Diagenesis of carbonate associated sulfate. Chem. Geol. 463, 61–75.

Geilert, S., Frick, D.A., Abbott, A.N., Löhr, S.C., 2024. Marine clay maturation induces systematic silicon isotope decrease in authigenic clays and pore fluids. Commun. Earth Environ. 5, 573.

Goldstein, R.H., 2001. Fluid inclusions in sedimentary and diagenetic systems. Lithos 55, 159–193.

Grathoff, G.H., Moore, D.M., 1996. Illite Polytype Quantification Using Wildfire© Calculated X-Ray Diffraction Patterns. Clays Clay Miner. 44, 835–842.

Haley, B.A., Du, J., Abbott, A.N., McManus, J., 2017. The Impact of Benthic Processes on Rare Earth Element and Neodymium Isotope Distributions in the Oceans. Front. Mar. Sci. 4, 1–12.

Han, S., Löhr, S.C., Abbott, A.N., Baldermann, A., Shields, G.A., Cui, H., Kaufman, A.J., Chen, B., Yu, B., 2024. Authigenic clay mineral constraints on spatiotemporal evolution of restricted, evaporitic conditions during deposition of the Ediacaran Doushantuo Formation. Earth Planet. Sci. Lett. 626, 118524.

Hassan, M.S., Baioumy, H.M., 2006. Structural and Chemical Alteration of Glauconite under Progressive Acid Treatment. Clays Clay Miner. 54, 491–499.

Hemming, S.R., Liu, T., Northrup, P., Nicholas, S., Rasbury, E.T., Chen, H., Warden, A., Chen, A., Li, R., Tappero, R., Cox, S.E., Everard, J., Wang, S., Deluca, M., Bostick, B., Halliday, A.N., 2023. Synchrotron microanalytical characterization and K/Ar dating of the GL-O-1 glauconite reference material at the single pellet scale and reassessment of the age of visually mature pellets. Minerals 13, 773.

Hille, M., Hu, Y., Huang, T.Y., Teng, F.Z., 2019. Homogeneous and heavy potassium isotopic composition of global oceans. Science Bulletin 64, 1740–1742.

Huang, W.L., Bishop, A.M., Brown, R.W., 1986. The effect of fluid/rock ratio on feldspar dissolution and illite formation under reservoir conditions. Clay Miner. 21, 585–601.

Huang, T.-Y., Teng, F.-Z., Rudnick, R.L., Chen, X.-Y., Hu, Y., Liu, Y.-S., Wu, F.-Y., 2020. Heterogeneous potassium isotopic composition of the upper continental crust. Geochim. Cosmochim. Acta 278, 122–136.

Isson, T.T., Planavsky, N.J., 2018. Reverse weathering as a long-term stabilizer of marine pH and planetary climate. Nature 560, 471–475.

Isson, T., Rauzi, S., 2024. Oxygen isotope ensemble reveals Earth's seawater, temperature, and carbon cycle history. Science 383, 666–670.

Jenkyns, H.C., 2010. Geochemistry of oceanic anoxic events. Geochem. Geophys. Geosyst. 11, Q03004.

Jones, C.E., Jenkyns, H.C., 2001. Seawater Strontium Isotopes, Oceanic Anoxic Events, and Seafloor Hydrothermal Activity in the Jurassic and Cretaceous. Am. J. Sci. 301, 112–149.

Kisiel, M., Skiba, M., Skoneczna, M., Maj-Szeliga, K., B łachowski, A., 2018. Weathering of glauconite in an alkaline environment – A case study from Krakow area, Poland. Catena 171, 541–551.

Krissansen-Totton, J., Catling, D.C., 2020. A coupled carbon-silicon cycle model over Earth history: Reverse weathering as a possible explanation of a warm mid-Proterozoic climate. Earth Planet. Sci. Lett. 537, 116181.

Legland, D., Kiêu, K., Devaux, M.-F., 2007. Computation of Minkowski measures on 2D and 3D binary images. Image Anal. Stereol. 26, 83–92.

Li, S., Li, W., Beard, B.L., Raymo, M.E., Wang, X., Chen, Y., Chen, J., 2019. K isotopes as a tracer for continental weathering and geological K cycling. Proc. Natl. Acad. Sci. USA 116, 8740–8745.

Li, W., Liu, X.-M., Wang, K., Fodrie, F.J., Yoshimura, T., Hu, Y.-F., 2021a. Potassium phases and isotopic composition in modern marine biogenic carbonates. Geochim. Cosmochim. Acta 304, 364–380.

Li, W., Lui, X.-M., Hu, Y., Teng, F.-Z., Hu, Y., 2021b. Potassium isotopic fractionation during clay adsorption. Geochim. Cosmochim. Acta 304, 160–177.

Li, W., Liu, X.-M., Wang, K., McManus, J., Haley, B.A., Takahashi, Y., Shakouri, M., Hu, Y., 2022. Potassium isotope signatures in modern marine sediments: Insights into early diagenesis. Earth Planet. Sci. Lett. 599, 117849.

Löhr, S.C., Khazaie, E., Farkaš, J., Baldermann, A., Gilbert, S., Maas, R., Subarkah, D., Blades, M.L., Collins, A.S., 2025. Origin and Significance of Age Variability in the Glauconite Reference Material GL-O: Implications for In Situ Rb-Sr Geochronology. Geostand. Geoanal. Res. 49, 197–216.

Löhr, S.C., Zheng, X.-Y., Farkaš, J., Lv, Y., Abbott, A.N., Baldermann, A., Weissgerber, J., 2026a. Marine clay authigenesis controls seawater potassium isotope composition. In review. Earth Planet. Sci. Lett.

Löhr, S.C., Abbott, A.N., Baldermann, A., Farkaš, J., 2026b. Impact of authigenic clay formation on marine trace element cycling. Accepted. Nat. Commun.

Loyola, C., Farkaš, J., Collins, A.S., Gilbert, S.E., Verdel, C., Löhr, S.C., Brock, G.A., Shields, G.A., Baldermann, A., Redaa, A., Blades, M., Subarkah, D., Bishop, C., Giles, S.H., Christie-Black, N., Haines, P.W., 2025. In situ Rb–Sr dating and REE analysis of glauconites and detrital feldspars from the Ediacaran/Cambrian strata: Centralian and Adelaide Superbasins, Australia. Precam. Res. 427, 107851.

Lyons, T.W., Tino, C.J., Fournier, G.P., Anderson, G.P., Leavitt, W.D., Konhauser, K.O., Stüeken, E.E., 2024. Co-evolution of early Earth environments and microbial life. Nat. Rev. Microbiol. 22, 572–586.

Maire, E., Withers, P.J., 2014. Quantitative X-ray tomography. Int. Mater. Rev., 59, 1–43.

MathWorks, 2025. MATLAB R2025b. The MathWorks, Inc., Natick, Massachusetts, USA.

Martin, J., Lusher, A., Nixon, F.C., 2022. A review of the use of microplastics in reconstructing dated sedimentary archives. Sci. Total Environ. 806, 150818.

McLachlan, G.J., Peel, D., 2000. Finite Mixture Models. New York: Wiley.

Mernagh, T.P., 2015. A Review of Fluid Inclusions in Diagenetic Systems. Bulletin of the Geological Society of China 89, 697–714.

Montagna, P., Silenzi, S., Devoti, S., Mazzoli, C., McCulloch, M., Scicchitano, G., Taviani, M., 2008. Climate reconstructions and monitoring in the Mediterranean Sea: A review on some recently discovered high-resolution marine archives. Rend. Fis. Acc. Lincei 19, 121–140.

Mosser-Ruck, R., Pironon, J., Cathelineau, M., Trouiller, A., 2001. Experimental illitization of smectite in a K-rich solution. Eur. J. Miner. 13, 829–840.

Müller, R.D., Mather, B., Dutkiewicz, A., Keller, T., Merdith, A., Gonzalez, C.M., Gorczyk, W., Zahirovic, S., 2022. Evolution of Earth’s tectonic carbon conveyor belt. Nature 605, 629–639.

Odin, G.S., 1982. Interlaboratory standards for dating purposes. In: Odin, G.S. (ed.), Numerical dating in stratigraphy. Wiley (New York), 123–150.

Odin, G.S., Matter, A., 1981. De glauconiarum origine. Sedimentology 28, 611–641.

Paytan, A., Kastner, M., Campbell, D., Thiemens, M.H., 1998. Sulfur Isotopic Composition of Cenozoic Seawater Sulfate. Science 282, 1459–1462.

Pestitschek, B., Gier, S., Essa, M., Kurzweil, H., 2012. Effects of Weathering on Glauconite: Evidence from The Abu Tartur Plateau, Egypt. Clays Clay Miner. 60, 76–88.

Prewitt, J.M.S., Mendelsohn, M.L., 1966. The analysis of cell images. Ann. N. Y. Acad. Sci. 128, 1035–1053.

Rafiei, M., Löhr, S.C., Alard, O., Baldermann, A., Farkaš, J., Brock, G.A., 2023. Microscale Petrographic, Trace Element, and Isotopic Constraints on Glauconite Diagenesis in Altered Sedimentary Sequences: Implications for Glauconite Geochronology. Geochem. Geophys. Geosyst. 24, e2022GC010795.

Richter, F.M., Rowley, D.B., DePaolo, D.J., 1992. Sr isotope evolution of seawater: the role of tectonics. Earth Planet. Sci. Lett. 109, 11–23.

Rubio, B., López-Pérez, A.E., 2024. Exploring the genesis of glaucony and verdine facies for paleoenvironmental interpretation: A review. Sed. Geol. 461, 106579.

Sánchez-Navas, A., Martín-Algarra, A., Eder, V., Jagannadha Reddy, B., Nieto, F., Zanin, Y.N., 2008. Color, mineralogy and composition of Upper Jurassic West Siberian glauconite: useful indicators of paleoenvironment. Can. Miner. 46, 1249–1268.

Santiago Ramos, D.P., Morgan, L.E., Lloyd, N.S., Higgins, J.A., 2018. Reverse weathering in marine sediments and the geochemical cycle of potassium in seawater: Insights from the K isotopic composition (^{41}K/^{39}K) of deep-sea pore-fluids. Geochim. Cosmochim. Acta 236, 1–22.

Scheiblhofer, E., Moser, U., Löhr, S., Wilmsen, M., Farkaš, J., Gallhofer, D., Bäckström, A.M., Zack, T., Baldermann, A., 2022. Revisiting Glauconite Geochronology: Lessons Learned from In Situ Radiometric Dating of a Glauconite-Rich Cretaceous Shelfal Sequence. Minerals, 12, 818.

Selby, D., 2009. U-Pb zircon geochronology of the Aptian/Albian boundary implies that the GL-O international glauconite standard is anomalously young. Cretaceous Research 30, 1263–1267.

Seton, M., Gaina, C., Müller, R.D., Heine, C., 2009. Mid-Cretaceous seafloor spreading pulse: Fact or fiction? Geology 37, 687–690.

Soille, P. Morphological Image Analysis: Principles and Applications. Berlin: Springer, 1999.

Sommer, C., Straehle, C., Köthe, U., Hamprecht, F.A., 2011. Ilastik: Interactive learning and segmentation toolkit. In: 2011 IEEE Int. Symp. Biomed. Imaging: From Nano to Macro. IEEE, 230–233.

Steffen, W., Richardson, K., Rockström, J., Schellnhuber, H.J., Dube, O.P., Dutreuil, S., Lenton, T.M., Lubchenco, J., 2020. The emergence and evolution of Earth System Science. Nat. Rev. Earth Environ. 1, 54–63.

Swart, P.K., 2015. The geochemistry of carbonate diagenesis: The past, present and future. Sedimentology 62, 1233–1304.

Teng, F.-Z., Hu, Y., Ma, J.-L., Wei, G.-J., Rudnick, R.L., 2020. Potassium isotope fractionation during continental weathering and implications for global K isotopic balance. Geochim. Cosmochim. Acta 278, 261–271.

Tribovillard, N., Bout-Roumazeilles, V., Guillot, F., Baudin, F., Deconinck, J.-F., Abraham, R., Ventalon, S., 2023. A sedimentological oxymoron: highly evolved glauconite of earliest diagenetic origin. C. R. Géosci. 355, 157–173.

Wanamaker Jr., A.D., Hetzinger, S., Halfar, J., 2011. Reconstructing mid- to high-latitude marine climate and ocean variability using bivalves, coralline algae, and marine sediment cores from the Northern Hemisphere. Palaeogeogr. Palaeoclimatol. Palaeoecol. 302, 1–9.

Wang, K., Close, H.G., Tuller-Ross, B., Chen, H., 2020. Global Average Potassium Isotope Composition of Modern Seawater. ACS Earth Space Chem. 4, 1010–1017.

Wang, K., Li, W., Li, S., Tian, Z., Koefoed, P., Zheng, X.-Y., 2021. Geochemistry and Cosmochemistry of Potassium Stable Isotopes. Geochem. 81, 125786.

Warren, J. K., 2010. Evaporites through time: Tectonic, climatic and eustatic controls in marine and nonmarine deposits. Earth-Sci. Rev. 98, 217–268.

Weaver, C.E., Pollard, L.D., 1973. The Chemistry of Clay Minerals, 213 pp. Elsevier, Amsterdam, London, New York.

Wilmsen, M., 2007. Accommodation- versus capacity-controlled deposition in the Cenomanian (Upper Cretaceous) of northern Germany. Beringeria 37, 239–251.

Wilmsen, M., Bansal, U., 2021. Depositional setting and limiting factors of early Late Cretaceous glaucony formation: implications from Cenomanian glauconitic strata (Elbtal Group, Germany). Facies 67, 24.

Wilmsen, M., Niebuhr, B., Hiss, M., 2005. The Cenomanian of northern Germany: facies analysis of a transgressive biosedimentary system. Facies 51, 242–263.

Winkelstein, I.Z., Lohmann, K.C., 2016. Shallow burial alteration of dolomite and limestone clumped isotope geochemistry. Geology 44, 467–470.

Zheng, X.-Y., Beard, B.L., Neuman, M., Fahnestock, M.F., Bryce, J.G., Johnson, C.M., 2022a. Stable potassium (K) isotope characteristics at mid-ocean ridge hydrothermal vents and its implications for the global K cycle. Earth Planet. Sci. Lett. 593, 117653.

Zheng, X.-Y., Chen, X.-Y., Ding, W., Zhang, Y., Charin, S., Gérard, Y., 2022b. High precision analysis of stable potassium (K) isotopes by the collision cell MC-ICP-MS “Sapphire” and a correction method for concentration mismatch. J. Anal. At. Spectrom. 37, 1273–1287.

Figures and Tables

Table 1: Mean composition (±2SD) of the bulk glauconite fractions (P4-P7) and separated glauconite sub-fractions (P6 sub-series) determined by EMP analysis.

Sample type	No. of spots	Data type	Al_2O_3 (wt.%)	MgO (wt.%)	SiO_2 (wt.%)	Na_2O (wt.%)	CaO (wt.%)	Fe_2O_3 (wt.%)	FeO (wt.%)	K_2O (wt.%)	P_2O_5 (wt.%)	Total (wt.%)
P4_1	37	mean	8.42	4.10	51.25	0.02	0.39	21.33	1.92	8.97	0.21	96.62
		2SD	0.61	0.17	1.34	0.02	0.81	0.81	0.07	0.29	0.43	1.11
P5	44	mean	6.95	4.07	51.28	0.03	0.40	23.16	2.08	8.96	0.23	97.17
		2SD	0.84	0.23	1.85	0.03	1.38	1.39	0.13	0.32	0.69	1.16
P6	37	mean	8.22	4.30	52.40	0.02	0.51	21.13	1.90	8.73	0.34	97.55
		2SD	0.88	0.22	1.39	0.02	0.57	1.40	0.13	0.23	0.78	1.36
P7	26	mean	7.74	4.29	52.68	0.03	0.13	22.16	2.00	9.19	0.10	98.31
		2SD	0.61	0.16	0.87	0.03	0.13	1.18	0.11	0.33	0.19	1.21
P6a	11	mean	9.68	4.35	53.96	0.33	0.35	18.24	2.73	6.94	0.22	96.81
		2SD	1.27	0.60	0.87	0.10	0.17	1.19	0.18	0.38	0.25	1.13
P6b	12	mean	7.16	4.32	52.71	0.17	0.25	20.58	3.63	7.42	0.30	96.54
		2SD	1.35	0.56	1.17	0.06	0.05	1.74	0.31	0.53	0.28	1.22
P6c	14	mean	11.46	4.02	57.91	0.30	0.26	17.17	2.19	4.12	0.13	97.55
		2SD	1.25	0.55	0.94	0.16	0.17	1.01	0.30	1.05	0.11	1.41
P6d	10	mean	9.49	4.18	54.74	0.24	0.29	18.64	3.09	6.35	0.26	97.29
		2SD	1.32	0.42	1.46	0.14	0.11	1.78	0.43	0.65	0.32	1.23

Table 2: Mean values (±1SD) of morphological descriptors determined by statistical analysis of CT-derived 3D image data of glauconite grains from the P6 sub-series. The '*' refers to the presence of oxidized rims of different thickness at the glauconite grain surfaces (cf. Fig. 1c).

Sample type	Total porosity (vol.%)	Inner porosity (vol.%)	Sphericity (-)	Mean pore volume (μm^3)	Inner pore volume (μm^3)	Average rust layer thickness (µm)*
Light green pellets (sample P6a)	10.1 ±8.1	10.9 ±9.9	0.75 ±0.11	27.1 ±9.1	24.3 ±17.4	4.5
Medium/dark green pellets (sample P6b)	1.8 ±0.6	1.3 ±1.4	0.73 ±0.03	15.7 ±10.9	9.2 ±10.7	4.7
Foraminifera test infills (sample P6c)	7.8 ±12.6	9.4 ±15.8	0.75 ±0.01	34.5 ±50.5	52.0 ±85.2	4.2
Oxidized grains (sample P6d)	4.4 ±2.5	1.0 ±0.3	0.74 ±0.02	27.8 ±23.9	7.5 ±8.2	10.2

Table 3: Mean δ^{41}K isotopic composition (±2SD) of the detrital/burial diagenetic clay fraction (samples P1-3), bulk glauconite fractions (samples P4-P7) and separated glauconite pellets (P6 sub-series).

Sample type	Description	δ^{41}K (‰)	2SD	n
P1	Ilt and Ilt-Smc	-0.46	0.05	5
P2	Ilt and Ilt-Smc	-0.51	0.02	5
P3	Ilt and Ilt-Smc	-0.51	0.04	4
P4_1	Glauconite grains	-0.65	0.03	5
P4_2	Glauconite grus	-0.71	0.05	4
P5	Glauconite grains	-0.68	0.04	5
P5a	Glauconite (< 1 µm)	-0.67	0.03	8
P6	Glauconite grains	-0.67	0.03	5
P6a	Light green grains	-0.67	0.02	5
P6b	Dark green grains	-0.68	0.05	5
P6c	Foraminifera test infills	-0.66	0.03	5
P6d	Oxidized grains	-0.71	0.04	4
P7	Glauconite grains	-0.64	0.05	7
GL-O_1	Dark green grains	-0.65	0.03	5
GL-O_2	Dark green cracked grains	-0.67	0.02	7
GL-O_3	Very dark green grains	-0.66	0.05	5
GL-O_4	Medium green grains	-0.65	0.03	5
GL-O_5	Medium green cracked grains	-0.80	0.02	5
GL-O_6	Light green grains	-0.63	0.03	5
GL-O_7	Weathered grains	-0.68	0.02	5

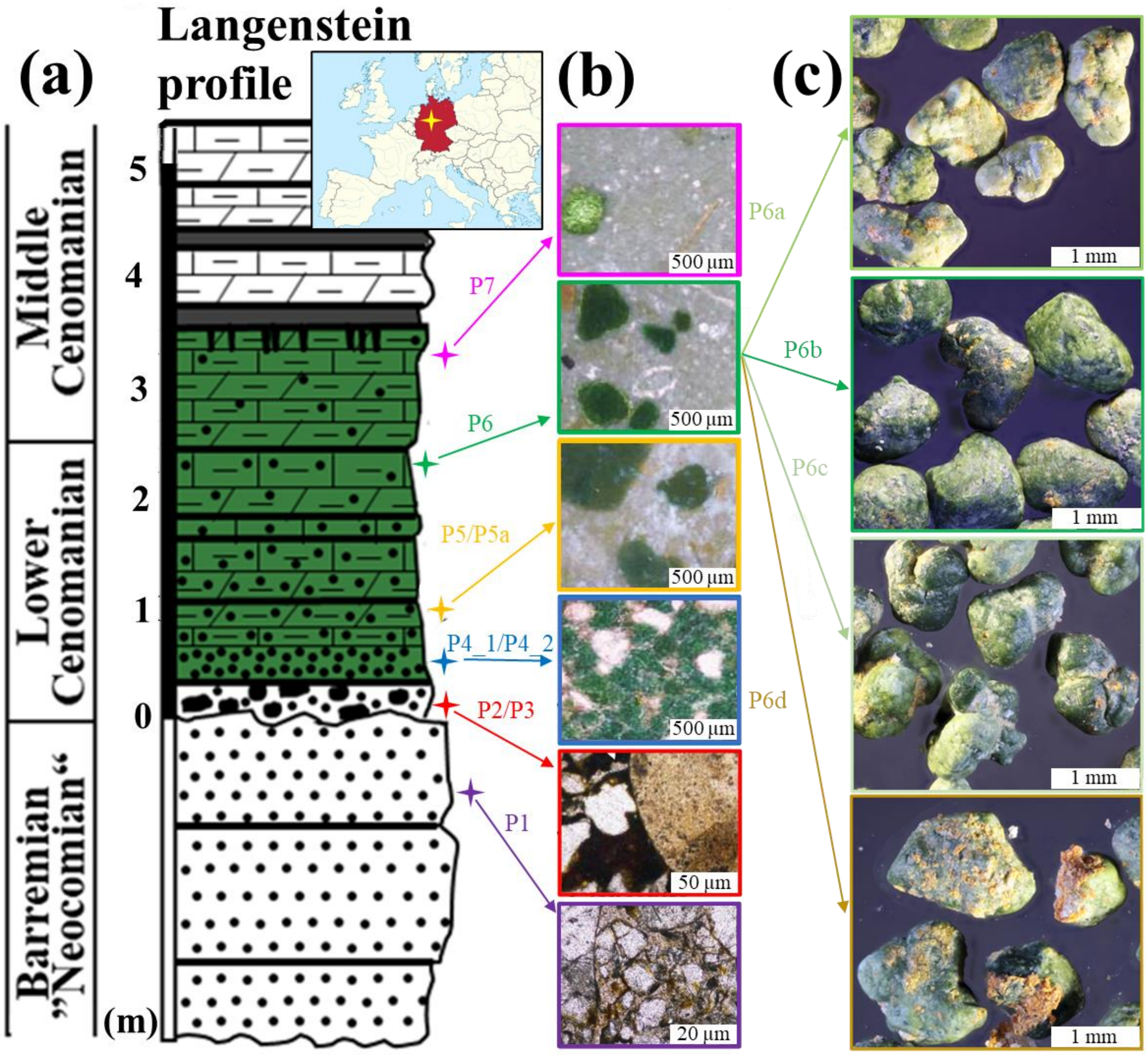

Figure 1: (a) Overview of the study site, where the yellow star marks the locality Langenstein in the Subhercynian Cretaceous Basin (Germany). The lithostratigraphic profile of Langenstein includes the glauconite-bearing interval colored in green. (b) Lithofacies at Langenstein (from bottom to top): Neocomian sandstone embedded in a clayey matrix (P1); conglomerate with apatite grains and hematite cement (P2 and P3); glauconite-bearing sandstone (P4_1 and P4_2); glauconitic mud- to packstones (P5-P7 and P5a). (c) Photomicrographs of separated green grain sub-fractions from sample P6 (from top to bottom): light green pellets (P6a), dark green pellets (P6b), foraminifer test infillings (P6c) and oxidized (weathered) pellets (P6d).

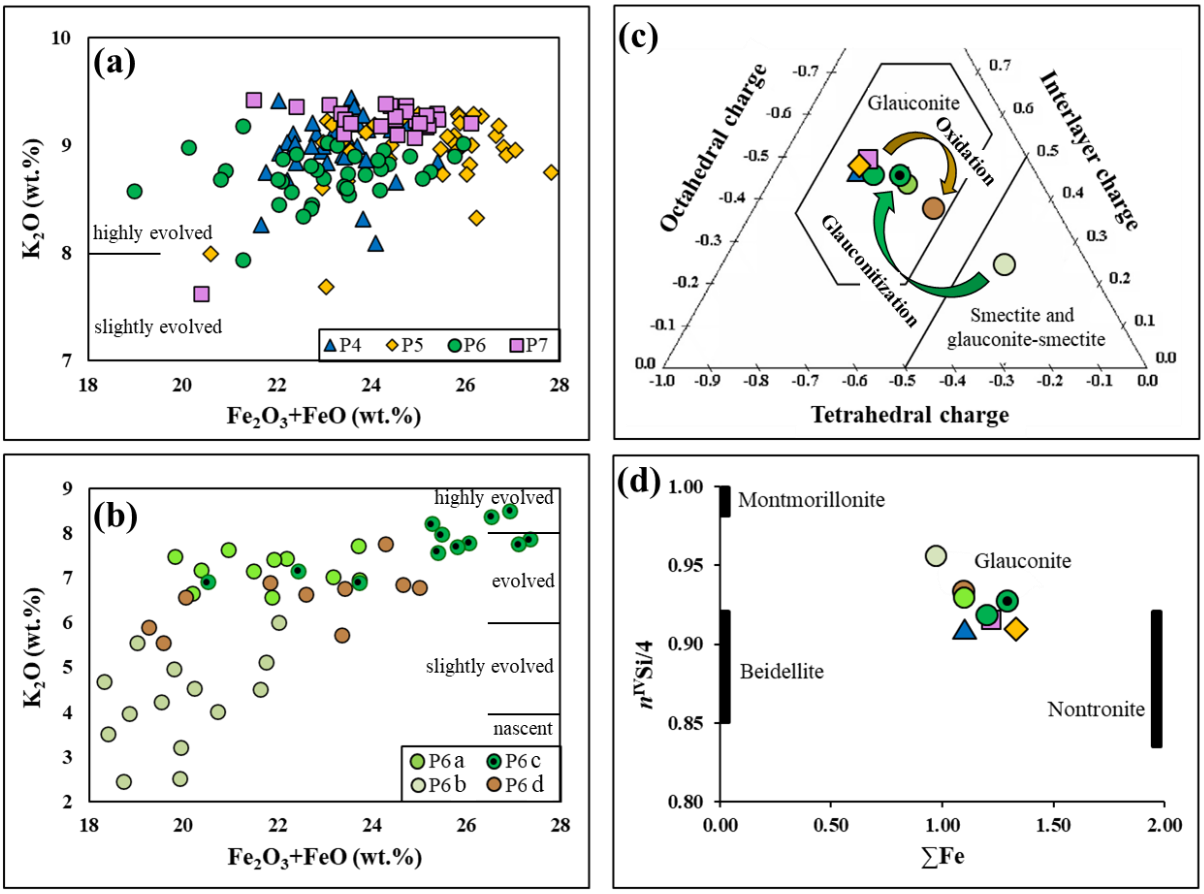

Figure 2: Chemical composition of glauconite and glauconite-smectite. (a,b) Cross-plot of K_2O vs total Fe content shows the green grains to be nascent to highly evolved and Fe-rich, which is typical of Mesozoic to Cenozoic glauconites. (c,d) The plot of the averaged chemical data in the charge distribution diagram and n^{IV}Si/4 vs total Fe content diagram identifies the green grains as glaucony members. Note that P6d grains follow reverse glauconitization.

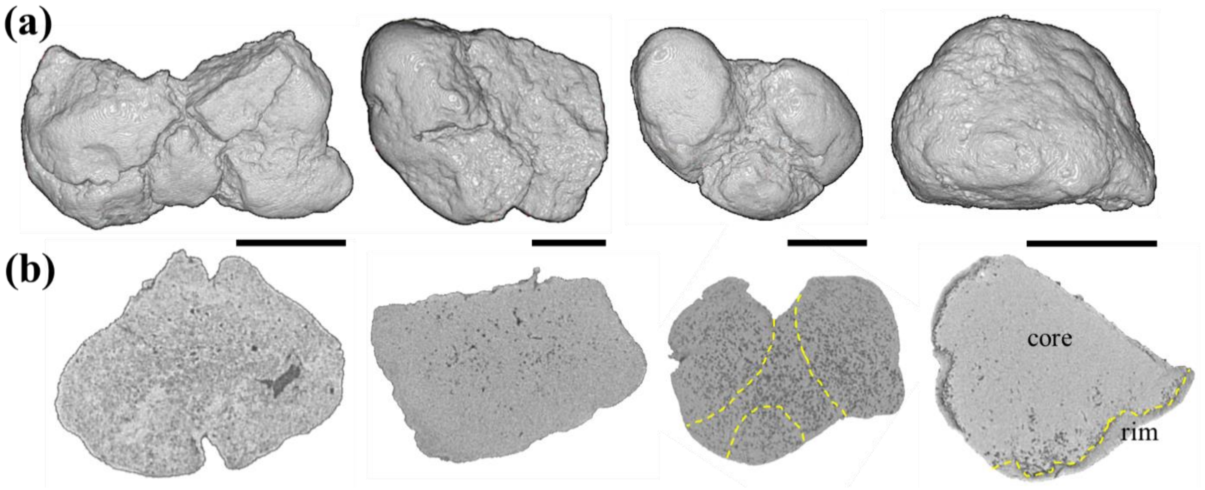

Figure 3: 3D images of selected glauconite pellets from sub-sample P6 show microstructural features based on processed CT image data in (a) from left to right: light green pellets, medium/dark green pellets, foraminifer test infillings (here: Hedbergella, with former chambers marked with dashed yellow lines) and oxidized (weathered) pellets and corresponding sections in (b). Scale bar: 200 µm. See Table 2 for mean values of morphological descriptors of the glauconites.

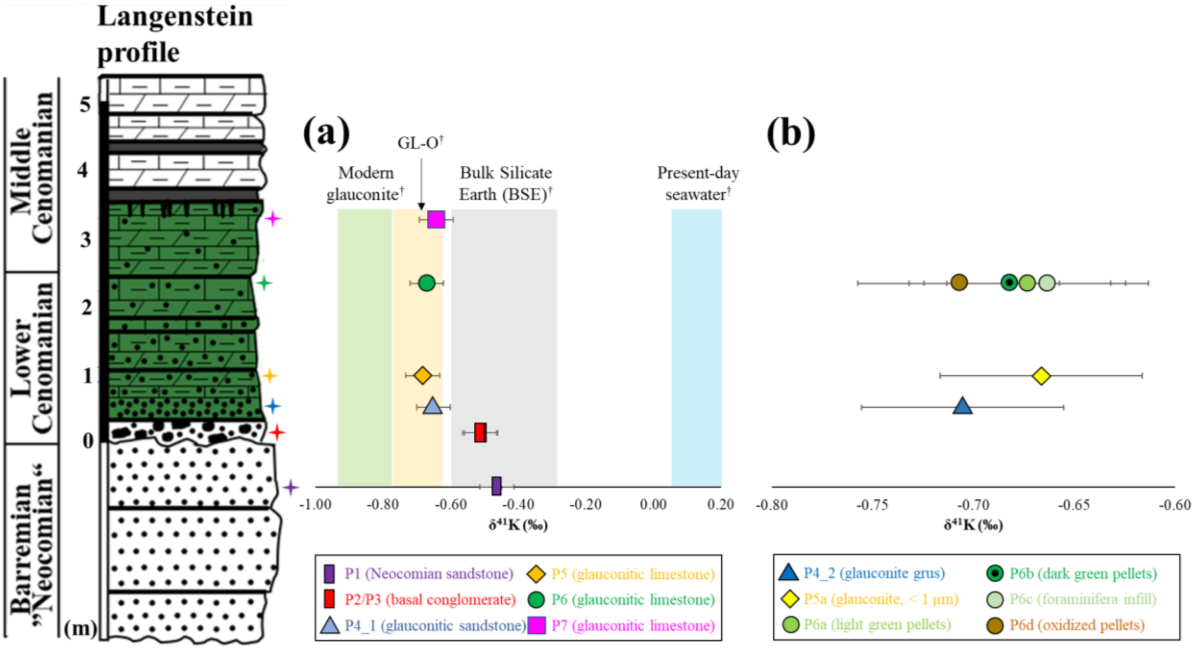

Figure 4: δ^{41}K isotope systematics observed across the Langenstein profile showing (a) the transition from continental detrital/burial diagenetic sedimentation to marine glauconite deposition and (b) the narrow δ^{41}K isotope range of glauconite separates from the P6 sub-series despite significant microstructural differences. The δ^{41}K compositions of modern glauconites (Löhr et al., submitted), present-day seawater (Wang et al., 2020), Bulk Silicate Earth (Wang et al., 2021) and GL-O are included for comparison.

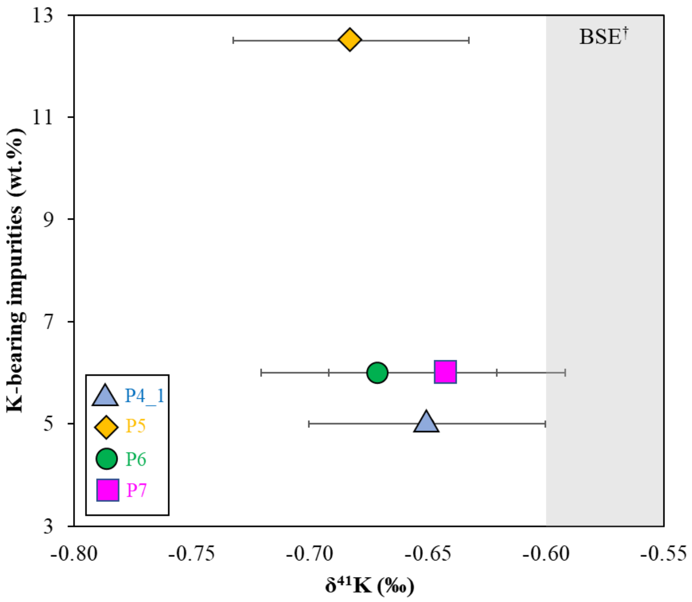

Figure 5: Content of K-bearing clay mineral impurities (i.e., detrital illite and burial diagenetic illite-smectite) in bulk glauconite fractions (data from Scheiblhofer et al., 2022) plotted against the glauconite $\delta^{41}K$ composition. Note the absence of a correlation. BSE (Wang et al., 2021) is included for comparison.

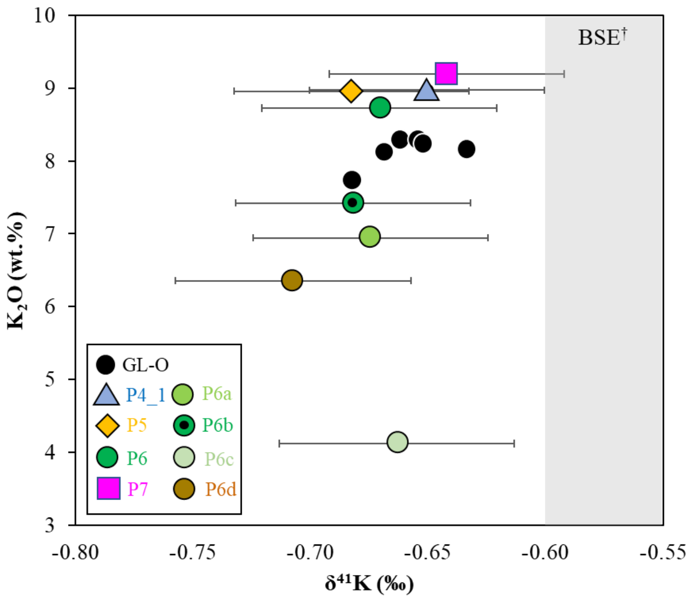

Figure 6: K_2O contents vs $\delta^{41}K$ isotope compositions of individual glauconite fractions from Langenstein (this study) and GL-O (data from Löhr et al., 2025). Note the absence of a correlation. BSE compositional range (Wang et al., 2021) is included for comparison.

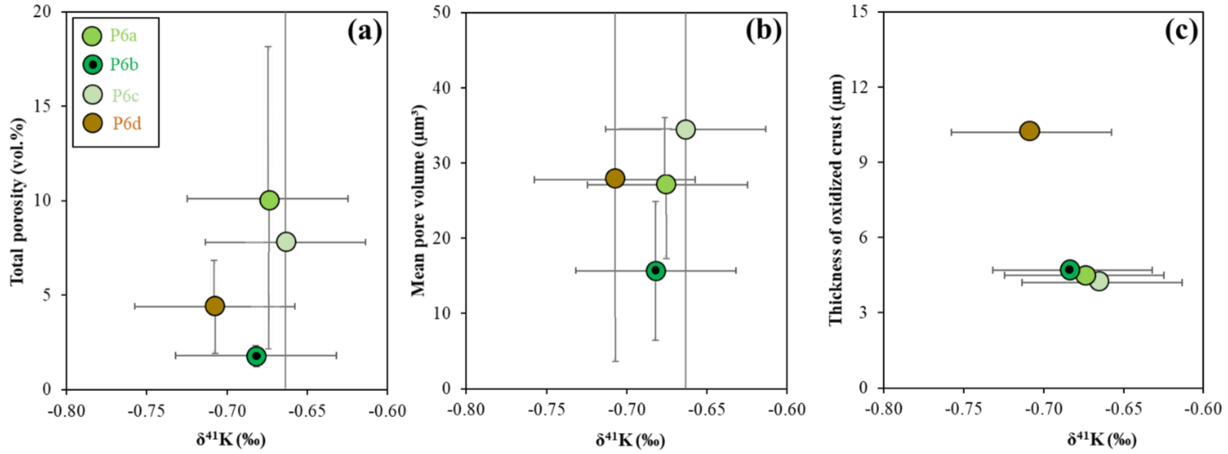

Figure 7: Effect of (a) total porosity, (b) mean pore volume and (c) thickness of oxidized surface crust on the δ^{41}K isotopic composition of glauconite separates from the P6 sub-series. Crust thicknesses have been obtained on a single grain, meaning no 1SD can be presented.

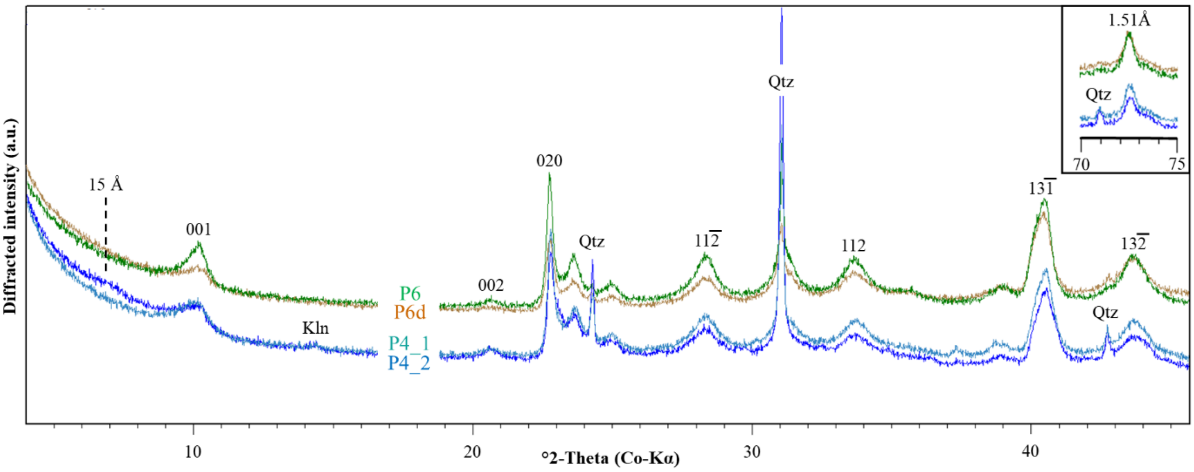

Figure 8: Effect of grain surface oxidation on the bulk mineralogical composition of extracted glauconite grains. Note the asymmetric broadening of the glauconite 001-reflection (sample P6d) and the appearance of a 15 Å-peak (sample P4_2) upon intensified chemical weathering, which point the reverse glauconitization.